Two-Phase Flow in Structured Packings: Modeling and Calculation on a Macroscopic Scale

B. Mahr
Bayer Technology Services GmbH, D-51368 Leverkusen, Germany

D. Mewes
Leibniz University of Hannover, Institute of Process Engineering, Callinstrasse 36, D-30167 Hannover, Germany

DOI 10.1002/aic.11400

A model is presented that allows calculating the macroscopic flow field of counter-current two-phase flow in strongly anisotropic porous structures. It is applied to corrugated structured packings. All flow field variables and packing properties are averaged over the volume of an elementary cell. The anisotropic gas flow resistance is derived from measurements and from separate CFD calculations on 3D-X-ray CT scans. The liquid's flow resistance is calculated using an analytical model of liquid film flow on an inclined plate. Liquid flow along both preferential flow directions is represented by two separate phases, in order to consider horizontal forces despite their symmetry. Gas-liquid momentum transfer above the loading point is included. The macroscopic flow field is calculated for a 288 mm I.D. column containing four packing elements. Liquid spreading from a point source, for uniform irrigation, increased hold-up at the packing elements' joints and pressure drop are tested against experimental results.

© 2008 American Institute of Chemical Engineers *AIChE J,* 54: 614–626, 2008
Keywords: CFD, structured packing, two-phase flow, elementary cell model, anisotropic pressure drop, X-ray, tomography

Introduction

For the separation of liquid mixtures columns equipped with trays or packed beds are used. A large interfacial area between gas and liquid is desirable for best heat and mass transfer. To maximize the driving force, highest mean temperature and concentration differences are achieved when the phases are conducted counter-currently through the apparatus.

As an alternative to conventional separation columns with trays or packed beds, structured packings have become increasingly popular. It has been estimated that 25% of all refinery vacuum towers worldwide are equipped with structured packing.[1] Structured packings are mostly made of corrugated sheets of metal or other materials. The layers of corrugated material are arranged with alternating orientation of the corrugation thus forming crossing open channels. The structure can be viewed as a regular porous body with large surface area and large void fraction. Compared with conventional dumped packings, structured packings feature lower pressure drop, higher separation efficiency, higher capacity, and better radial mixing. Because of their structure of crossing channels, they show strong preferential flow directions for both liquid and gas flow. When operated in two-phase flow, these preferential flow directions and the low pressure drop causes structured packings to be more susceptible to maldistribution of the phases and instabilities in the flow field, which in turn leads to poor column performance. For equipment design, scale-up and operation it is therefore desirable to gain better understanding of the hydrodynamics in structured packings, and to be able to predict flow fields and operational ranges in those columns.[2,3]

There have been many approaches to model multiphase flow in packed columns. A large number of one-dimensional models (i.e., assuming constant phase and velocity distribution over

---

Correspondence concerning this article should be addressed to B. Mahr at bastian.mahr@gmx.de or D. Mewes at mewes@ifv.uni-hannover.de.

cross-section and height of the column) have been developed to predict pressure drop, liquid hold-up, and mass transfer in packed columns both from empirical and mechanistic points of view.[1,4–10] The models differ in the way e.g., empirical correlations, geometric features of the packing, partial wetting, interphase momentum transfer or the interaction between momentum and mass transfer are taken into account. The prediction of liquid hold-up is usually based on the consideration of liquid films on inclined plates or in pipes.[8] Brauer[11] derives an analytical model for gas-liquid flow in vertical pipes. Assuming laminar film flow it allows calculating liquid film thickness as a function of the interphase shear stress without empirical correlations.

Stoter et al.[12] model the three-dimensional gas flow field in corrugated structured packing by dividing the packing into cells and solving mass, momentum, and energy balances. Stoter[13] calculates the liquid distribution in structured packings. On the basis of experimental data he models the split-up of liquid between cells by solving only the mass balances. Jiang et al.[14,15] calculate the steady-state flow field based on the minimization of energy dissipation. A neural network approach was used by Iliuta et al.[16] to model hydrodynamics and gas-liquid mass transfer in trickle bed reactors based on extensive measurement data from the open literature. Mewes et al.[17] adapted the elementary cell model by Arbogast et al.[18] to model two-phase flow in monoliths consisting of parallel channels. They solve volume-averaged mass and momentum equations to calculate the instable flow field and are able to capture liquid maldistribution and recirculation.

Recently, CFD has been used to calculate the local flow field of single-phase flow through the exact geometry of triangular channels of a corrugated structured packing[19] and packed beds of spheres.[20] Zhang[21] compares different turbulence models for gas flow through a cross-corrugated membrane including heat transfer. The exact path and break-up of liquid films and rivulets on a section of packing has been calculated by Hoffmann et al.[22] Currently, these approaches using the exact packing geometry are only feasible for either gas or liquid flow and for small segments of packed beds only. Modeling two-phase flow at the scale of the exact packing geometry is not yet feasible for columns of technical dimensions with today's computing power.

Effects like large scale maldistribution and instabilities in the flow field can only be modeled, though, if hydrodynamics of the entire column are taken into account. In the present study, the macroscopic three-dimensional flow field of an entire column is modeled and numerically calculated. The 288 mm I.D. column contains four elements of structured packing rotated against each other by 90°. It is a mechanistic model based on the elementary cell model by Mewes et al.,[17] but extended to be used on the anisotropic porous structure of corrugated structured packings. It allows calculating steady-state and dynamic two-phase flow fields under counter-current operating conditions below and above the loading point. The modeled phases are water and air. The results are tested against X-ray radiographic measurements.

The Elementary Cell Model for Structured Packings

Arbogast et al.[18] developed a mathematical model to calculate flow in porous media. Its extension to two-phase flow including a detailed derivation is given by Mewes et al.[17] The model is based on the idea that the entire porous structure can be subdivided into elementary cells. An elementary cell is a representative volume typically comprising several pores. The local variable values within an elementary cell, such as velocity, phase fraction, flow resistance and pressure drop, are volume-averaged by formulating the conservation equations for mass and momentum for the scale of one elementary cell. The mass and momentum balances for the entire media are then set up based on volume-averaged variable values. Its' numerical solution provides the macroscopic flow field at the scale of the entire porous structure. Thus, the exact geometry of the pores does not have to be modeled and the local flow field within each elementary cell does not have to be known. One of the model's advantages is that a relatively coarse numerical mesh (one or few nodes per elementary cell) is sufficient, thus making calculation of technical scale columns feasible.

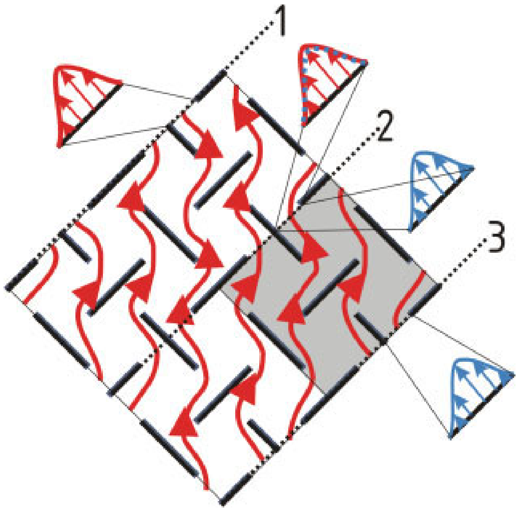

Figure 1. Schematic of four elementary cells in a section of structured packing with local velocity profiles at the cells' boundaries.

[Color figure can be viewed in the online issue, which is available at www.interscience.wiley.com.]

Applied to corrugated structured packings, an elementary cell is the smallest structure that is recurring periodically in all three dimensions. In Figure 1, four elementary cells and velocity profiles at their boundaries are shown schematically. Although the local velocity varies a lot within the elementary cell, the velocity profiles at opposite boundaries are almost identical. This illustrates why—in order to describe the macroscopic flow field within a column with structured packing—it is sufficient to model the flow field at periodic intervals only. For the elementary cell model, a superficial velocity is defined through a cutting plane A_k of an elementary cell. For each phase i the superficial velocity $\vec{j}_i = \bar{\alpha}_i \vec{\bar{v}}_i$ is given by

$$\vec{j}_i \cdot \bar{n} \equiv \frac{\int_{A_k} \alpha_i \vec{v}_i \cdot \vec{n}\, dA}{A_k}, \qquad (1)$$

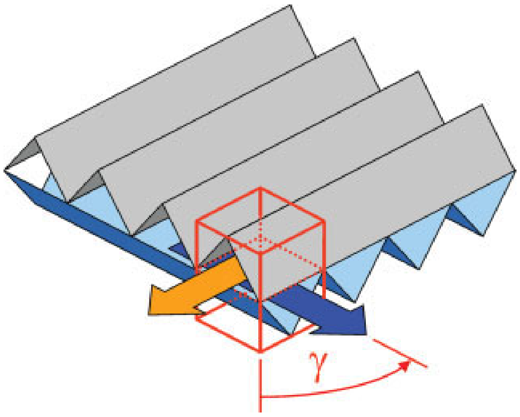

Figure 2. Schematic of two sheets of corrugated structured packing material.

An elementary cell and preferential flow directions through it are indicated. [Color figure can be viewed in the online issue, which is available at www.interscience.wiley.com.]

where $\vec{j}_i \cdot \vec{n}$ is the superficial velocity normal to A_k and the index k refers to the coordinate direction, $\vec{v}_i$ is the local velocity and α_i is the local volume fraction of phase i.

In Figure 2, a segment of packing is shown schematically and the volume of one elementary cell is indicated. Because of the periodicity requirement, an elementary cell must include two sheets of corrugated packing material. The layers of channels formed by the packing material feature two preferential flow directions within one elementary cell, which are indicated by arrows in Figure 2. The angle γ is measured from the vertical column axis. All variables of the flow field, e.g., phase fraction and velocity, are averaged over the volume of one elementary cell. Assuming similar velocities and phase fractions in both channel layers, all horizontal vector components cancel out. Thus, the average velocity over the entire elementary cell adds up to purely vertical flow. Equally, the horizontal forces exerted from the packing onto the fluid for both channel layers are symmetric with respect to the vertical. They as well add up to zero when averaged over an elementary cell. Because of this symmetry and the inclusion of two preferential flow directions in one elementary cell, horizontal spreading especially of the liquid phase cannot be captured with just one average velocity vector per phase and elementary cell.

Below the loading point, the flow field of the liquid phase is almost exclusively governed by gravity and the resulting forces between packing and liquid. The strong horizontal spreading induced by the preferential flow directions is an essential property of corrugated structured packings. It, therefore, cannot be neglected neither for regular steady-state operating conditions nor for possibly arising instabilities in the flow field.

Loser[23] used the elementary cell model for two-phase flow through dumped and structured packings with a diffusion model to capture the radial spreading. Though well suited for dumped packing with isotropic properties, the diffusion model cannot capture the strong anisotropy of corrugated structured packings.

In the current study, to model the horizontal forces between packing and liquid separately for both channel layers, the physically homogeneous liquid phase is split up into two liquid phases. Each liquid phase represents flow along one sheet of packing i.e., one preferential flow direction. For the model, the two liquid phases are treated as interpenetrating fluids which are both present in one elementary cell, but with different forces acting upon each of them. A set of mass and momentum conservation equations is formulated for each modeled liquid phase. Mass and momentum exchange between both modeled liquid phases is accounted for by specific expressions.

In contrast to the liquid phase, the flow field of the gas phase is mainly driven by the pressure gradient. The influence of gravity can be neglected. Besides, mass exchange between both preferential flow directions is greater than for the liquid phase. Therefore, the gas phase is described by one set of mass and momentum balances only. The anisotropic structure of the packing is modeled via a pressure drop coefficient that depends on the direction and magnitude of the gas velocity.

Altogether, the presented model employs three sets of conservation equations (one for each liquid phase and one for the gas phase) to calculate the macroscopic two-phase flow field of physically one liquid and one gas phase. Because of the large void fraction of structured packings and since the packing is immobile, the solid packing material is not modeled as a separate phase. This helps to reduce computational complexity.

A detailed derivation of the model equations can be found in Mahr[24] and Mahr and Mewes.[25,26] The main ideas, expressions, and resulting equations will be given in the following paragraphs.

Mass balances

The integral mass balances for any control volume V are written, assuming incompressibility of all three modeled phases. Formulating the mass balances for a large control volume including many elementary cells, the product of local velocity and local phase fraction can be substituted piecewise by the average superficial velocity defined by Eq. 1. Using the Gaussian theorem, these mass balances for the scale of the entire packing are transformed into their differential form

$$\nabla \vec{j}_{\mathrm{g}} = 0 \tag{2}$$

$$\nabla \vec{j}_{\mathrm{l1}} = \dot{v}_{\mathrm{l1}\to\mathrm{l2}} \tag{3}$$

$$\nabla \vec{j}_{\mathrm{l2}} = -\dot{v}_{\mathrm{l1}\to\mathrm{l2}} \tag{4}$$

$$\text{with } \dot{v}_{\mathrm{l1}\to\mathrm{l2}} = \frac{K(\bar{\alpha}_{\mathrm{l1}} - \bar{\alpha}_{\mathrm{l2}})}{\Delta t}, \tag{5}$$

where the subscripts g, l1, and l2 denote gas phase, liquid phase one and liquid phase two, respectively. $\vec{j}$ stands for the superficial velocity vector of the phase, and $\bar{\alpha}$ is the phase volume fraction averaged over the volume of an elementary cell V_{EC}.

$$\bar{\alpha}_i \equiv \frac{\int_{V_{\mathrm{EC}}} \alpha_i dV}{V_{\mathrm{EC}}}. \tag{6}$$

In Eqs. 3–5, $\dot{v}_{l1\rightarrow l2}$ refers to the effective, volume specific mass exchange between the two modeled liquid phases. Δt is the mean residence time of the liquid phases within a volume element. The effective mass exchange between the two modeled liquid phases is assumed to depend linearly on their difference in volume fractions. Within the packing, the linear coefficient K represents the contact area fraction between two adjacent sheets of packing. From 3D X-ray tomographic scans of the irrigated packing[24] it is estimated to be $K = 0.025$. This means that 2.5% of the difference in volume fraction of the two liquid phases is transferred in each elementary cell. At the column wall and at the joints where packing elements are stacked on top of each other, the exchange coefficient is chosen as 0.5. This results in equilibration of the liquid volume fractions of both phases. At the wall, this reflects a redirection of the liquid from the channel layer towards the wall to the adjacent channel layer away from the wall. Wall flow due to a gap between packing and column wall is not specifically accounted for, since wall flow depends strongly on the gap size, wall wipers, etc. At the packing elements' joints, an equilibration of liquid volume fractions model an equal split of all liquid between the two channel layers of the downstream packing element.

By summation of Eqs. 3 and 4 for both liquid phases

$$\nabla\vec{j}_{l1} + \nabla\vec{j}_{l2} = \nabla\vec{j}_{l} = 0 \qquad (7)$$

one receives Eqs. 2 and 7 which are very similar to the standard continuity equations for incompressible, steady-state two-phase flow. The only difference is that they use volume-averaged quantities, and their phase fractions do not add up to one, but to the average void fraction of the packing.

Momentum balance for the gas phase

Neglecting mass transfer between gas and liquid phase, the integral momentum balance for the gas phase for any control volume V can be written as

$$\begin{aligned}\frac{\partial}{\partial t}\int_V \alpha_g\rho_g\vec{v}_g\,dV + \oint_{\Gamma(V)} \alpha_g\rho_g(\vec{v}_g\vec{v}_g)dA &= -\int_V \alpha_g\nabla p\,dV - \oint_{\Gamma(V)} \alpha_g\,\underline{\underline{\tau_g}}\cdot\vec{n}\,dA \\ &\quad - \int_{A_{gp}} \underline{\underline{\sigma_g}}\cdot\vec{n}\,dA - \int_{A_{gl}} \underline{\underline{\sigma_g}}\cdot\vec{n}\,dA + \int_V \alpha_g\rho_g\vec{g}\,dV \qquad (8)\end{aligned}$$

where ρ_g stands for the gas density, $\Gamma(V)$ for the surface of the control volume V and $\underline{\underline{\tau_g}}$ is the shear stress tensor at the boundary of the control volume. The tensor $\underline{\underline{\sigma_g}}$ represents both pressure and shear stress on the gas phase within the control volume, with A_{gp} being the surface between gas and packing, i.e., the unwetted packing surface, and A_{gl} the phase boundary between gas and liquid. $\vec{g}$ stands for gravity. In Eq. 8 the first expression on the left hand side is the time-derivative of momentum and the second expression for the convective momentum transport. On the right hand side the first expression describes the forces due to a pressure gradient in the flow field, the second expression refers to viscous momentum transfer at the boundary of the control volume and the third and fourth expressions to momentum transfer between gas and packing and gas and liquid, respectively.

For the elementary cell, periodic boundary conditions can be assumed since the velocity profiles at opposite sides of the elementary cell are almost identical (see Figure 1). For the scale of the entire packing, the convective and viscous momentum transfer at the boundary of the control volume is far smaller than the friction between packing and gas. Thus, for both scales the second expression on the left and the second expression on the right hand side of Eq. 8 can be neglected. Because of the low gas density, the gravitational force described by the fifth expression on the right is neglected as well.

With the above assumptions and substituting averaged for local quantities, Eq. 8 reduces to

$$\begin{aligned}\frac{\partial}{\partial t}\int_V \bar{\alpha}_g\rho_g\bar{\vec{v}}_g\,dV &= -\int_V \bar{\alpha}_g\nabla\bar{p}\,dV \\ &\quad - \int_{A_{gp}} \underline{\underline{\sigma_g}}\cdot\vec{n}\,dA - \int_{A_{gl}} \underline{\underline{\sigma_g}}\cdot\vec{n}\,dA \qquad (9)\end{aligned}$$

For steady-state flow, the expression on the left can be set to zero and Eq. 9 then describes how pressure drop and forces between gas and packing and between gas and liquid, respectively, are in equilibrium. Writing the pressure drop as a linearized function of the gas superficial velocity, a simple relationship is derived,

$$\underline{\underline{\pi}}\cdot\vec{j}_g \equiv \bar{\alpha}_g\nabla\bar{p} = -\frac{\int_{A_{gp,EC}}\underline{\underline{\sigma_g}}\cdot\vec{n}\,dA + \int_{A_{gl,EC}}\underline{\underline{\sigma_g}}\cdot\vec{n}\,dA}{V_{EC}}. \qquad (10)$$

Equation 10 describes the forces between gas and packing and between gas and liquid averaged over the volume of an elementary cell V_{EC} as a function of the averaged superficial velocity in an elementary cell (see Eq. 1) and the flow resistance tensor $\underline{\underline{\pi}}$. The flow resistance tensor $\underline{\underline{\pi}}$ is a function of the direction of the gas velocity to model the anisotropic packing structure. The tensor also depends on the magnitude of the velocity, since the relationship between pressure and velocity is usually nonlinear.

The volume-averaged momentum transfer between gas and liquid can be separately written as

$$\vec{D}_{gl} \equiv -\frac{\int_{A_{gl,EC}}\underline{\underline{\sigma_g}}\cdot\vec{n}\,dA}{V_{EC}} \qquad (11)$$

Thus, the momentum balance for the gas phase Eq. 9 can be written in its differential form as

$$\frac{\partial}{\partial t}(\bar{\alpha}_g\rho_g\bar{\vec{v}}_g) = -\bar{\alpha}_g\nabla\bar{p} + \underline{\underline{\pi}}\cdot\vec{j}_g. \qquad (12)$$

Momentum balances for the liquid phase

As described before, two sets of momentum balances are formulated for the liquid phase in order to model flow in both channel layers of one elementary cell separately. The two integral momentum balances for liquid phase one and two with subscripts l1 and l2, respectively, are

$$\frac{\partial}{\partial t}\int_V \alpha_{l1}\rho_l\vec{v}_{l1}\,dV + \oint_{\Gamma(V)} \alpha_{l1}\rho_l(\vec{v}_{l1}\vec{v}_{l1})dA$$
$$= -\int_V \alpha_{l1}\nabla p\,dV - \oint_{\Gamma(V)} \alpha_{l1}\,\underline{\underline{\tau_{l1}}}\cdot\vec{n}\,dA - \int_{A_{l1p}} \underline{\underline{\sigma_{l1}}}\cdot\vec{n}\,dA$$
$$- \int_{A_{gl1}} \underline{\underline{\sigma_{l1}}}\cdot\vec{n}\,dA + \int_V \alpha_{l,1}\rho_l\vec{g}\,dV - \int_V \rho_l\dot{v}_{l1\to l2}\bar{\vec{v}}_t\,dV \qquad (13)$$

$$\frac{\partial}{\partial t}\int_V \alpha_{l2}\rho_l\vec{v}_{l2}\,dV + \oint_{\Gamma(V)} \alpha_{l2}\rho_l(\vec{v}_{l2}\vec{v}_{l2})dA$$
$$= -\int_V \alpha_{l2}\nabla p\,dV - \oint_{\Gamma(V)} \alpha_{l2}\,\underline{\underline{\tau_{l2}}}\cdot\vec{n}\,dA - \int_{A_{l2p}} \underline{\underline{\sigma_{l2}}}\cdot\vec{n}\,dA$$
$$- \int_{A_{gl2}} \underline{\underline{\sigma_{l2}}}\cdot\vec{n}\,dA + \int_V \alpha_{l2}\rho_l\vec{g}\,dV - \int_V \rho_l\dot{v}_{l1\to l2}\bar{\vec{v}}_t\,dV \qquad (14)$$

The integration is carried out over a control volume V with the outer surface $\Gamma(V)$. ρ_l stands for the liquid density, $\underline{\underline{\tau_{l1}}}$ and $\underline{\underline{\tau_{l2}}}$ are the tensors of the shear stresses at the control volume's boundary, and $\underline{\underline{\sigma_{l1}}}$ and $\underline{\underline{\sigma_{l2}}}$ are the pressure and shear stresses between packing or gas and one of the liquid phases. A_{l1p} and A_{l2p} are the surface areas wetted by the respective phase, and A_{gl1} and A_{gl2} are the phase boundaries between gas and the respective liquid phase. Viscous momentum transfer between the liquid phases is neglected, since each liquid phase represents flow on a different sheet of packing with little interaction between them. The last expression on the right hand side of Eqs. 13 and 14 stands for the convective momentum transfer associated with the effective mass transfer between the liquid phases. The average velocity $\bar{\vec{v}}_t$ is the one of the phase that is effectively transferring.

In general, the same assumptions are made for the liquid phases as for the gas phase, only gravity cannot be neglected for the liquid phase. Similar to Eq. 9 for the gas phase, Eqs. 13 and 14 simplify to

$$\frac{\partial}{\partial t}\int_V \alpha_{l1}\rho_l\vec{v}_{l1}\,dV = -\int_V \alpha_{l1}\nabla p\,dV - \int_{A_{l1p}} \underline{\underline{\sigma_{l1}}}\cdot\vec{n}\,dA$$
$$- \int_{A_{gl1}} \underline{\underline{\sigma_{l1}}}\cdot\vec{n}\,dA + \int_V \alpha_{l1}\rho_l\vec{g}\,dV - \int_V \rho_l\dot{v}_{l1\to l2}\bar{\vec{v}}_t\,dV \qquad (15)$$

$$\frac{\partial}{\partial t}\int_V \alpha_{l2}\rho_l\vec{v}_{l2}\,dV = -\int_V \alpha_{l2}\nabla p\,dV - \int_{A_{l2p}} \underline{\underline{\sigma_{l2}}}\cdot\vec{n}\,dA$$
$$- \int_{A_{gl2}} \underline{\underline{\sigma_{l2}}}\cdot\vec{n}\,dA + \int_V \alpha_{l2}\rho_l\vec{g}\,dV - \int_V \rho_l\dot{v}_{l1\to l2}\bar{\vec{v}}_t\,dV \qquad (16)$$

The second and third expression on the right hand side of Eqs. 15 and 16 describes the momentum transfer between packing, gas and the respective liquid phase. In analogy to Eq. 10 for the gas phase, this expression is written as a linearized function of phase i's liquid superficial velocity and a liquid flow resistance tensor $\underline{\underline{\xi_i}}$ defined by

$$\underline{\underline{\xi_1}}\cdot\vec{j}_{l1} \equiv \frac{\int_{A_{l1p,EC}} \underline{\underline{\sigma_{l1}}}\cdot\vec{n}\,dA + \int_{A_{gl1,EC}} \underline{\underline{\sigma_{l1}}}\cdot\vec{n}\,dA}{V_{EC}} \qquad (17)$$

$$\underline{\underline{\xi_2}}\cdot\vec{j}_{l2} \equiv \frac{\int_{A_{l2p,EC}} \underline{\underline{\sigma_{l2}}}\cdot\vec{n}\,dA + \int_{A_{gl2,EC}} \underline{\underline{\sigma_{l2}}}\cdot\vec{n}\,dA}{V_{EC}}. \qquad (18)$$

The momentum transport only between gas and liquid has already been introduced by Eq. 11. Both liquid phases contribute to it as expressed by

$$\vec{D}_{gl} = \vec{D}_{gl1} + \vec{D}_{gl2} = \frac{\int_{A_{gl1,EC}} \underline{\underline{\sigma_{l1}}}\cdot\vec{n}\,dA + \int_{A_{gl2,EC}} \underline{\underline{\sigma_{l2}}}\cdot\vec{n}\,dA}{V_{EC}} \qquad (19)$$

The volume-averaged convective momentum transfer due to the mass transfer between the liquid phases is written as

$$\vec{D}_{l1\to l2} \equiv \frac{\int_{V_{EC}} \rho_l\dot{v}_{l1\to l2}\bar{\vec{v}}_t\,dV}{V_{EC}}. \qquad (20)$$

Using Eqs. 17–20, the momentum balances for the liquid phases Eqs. 15 and 16 can be written in their differential form

$$\frac{\partial}{\partial t}(\alpha_{l1}\rho_l\vec{v}_{l1}) = -\bar{\alpha}_{l1}\nabla\bar{p} - \underline{\underline{\xi_1}}\cdot\vec{j}_{l1} + \bar{\alpha}_{l1}\rho_l\vec{g} - \vec{D}_{l1\to l2} \qquad (21)$$

$$\frac{\partial}{\partial t}(\alpha_{l2}\rho_l\vec{v}_{l2}) = -\bar{\alpha}_{l2}\nabla\bar{p} - \underline{\underline{\xi_2}}\cdot\vec{j}_{l2} + \bar{\alpha}_{l2}\rho_l\vec{g} + \vec{D}_{l1\to l2} \qquad (22)$$

Compared with Eq. 12 for the gas phase, Eqs. 21 and 22 for the liquid phases include gravitational forces and an expression accounting for the convective momentum transfer associated with the mass transfer between the liquid phases. The second expression on the right hand side including the momentum transfer between gas and liquid phase is especially important in the loading regime. The first expression containing the pressure gradient gains importance only near the flood point.

At the joint between two packing elements, each liquid phase is assumed to split evenly between both preferential flow directions, i.e., both liquid phases, in the downstream element. This has to be accounted for by appropriate boundary conditions or exchange terms at the packing elements' joints both for mass flux (see Eqs. 3 and 4) and similarly for momentum flux.

Anisotropic gas flow resistance

The momentum transport between packing, liquid phases and gas phase is described by the gas flow resistance tensor $\underline{\underline{\pi}}$ in Eq. 12. If no liquid is present, this is the dry pressure drop averaged over one elementary cell. As mentioned earlier, it should be noted in Figure 2, that one elementary cell includes two adjacent sheets of packing, i.e., one pair of

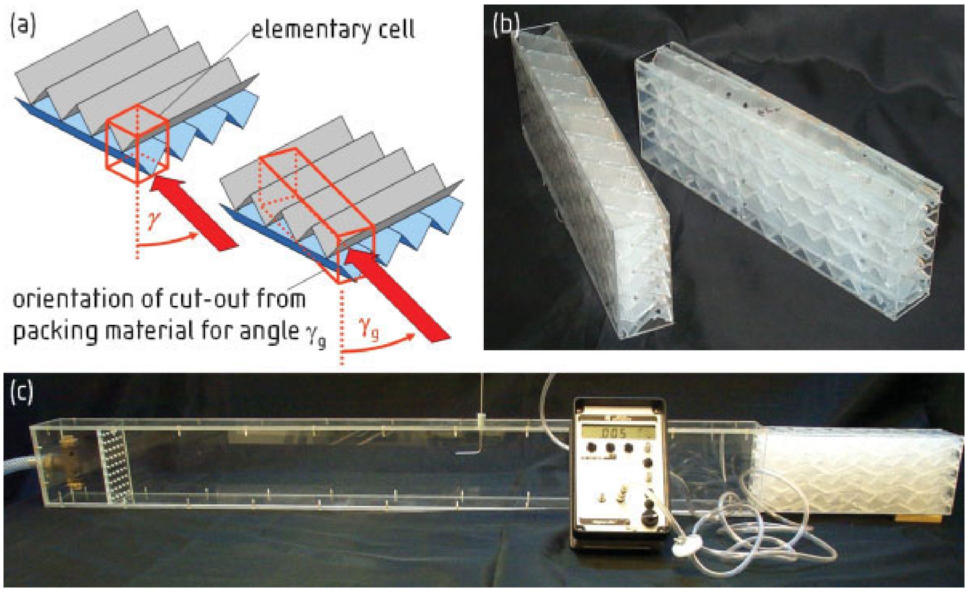

Figure 3. (a) Orientation of cut-outs from packing material, (b) photograph of cut-outs, (c) photograph of experimental rig for pressure drop measurements.

[Color figure can be viewed in the online issue, which is available at www.interscience.wiley.com.]

crossing channels. Because of this channel structure, the pressure drop within the packing is highly anisotropic: it depends not only on the gas velocity, but also on the flow direction of the gas. Within the plane of the sheets of packing, the angle γ is measured from the vertical column axis as indicated in Figure 2. Along the channels ($\gamma = \pm 42°$), pressure drop is expected to be lower than along the vertical column axis ($\gamma = 0°$), since the gas flow path is much more tortuous then. To measure the directional pressure drop within the packing sheet plane, sections of packing material (SULZER MELLAPAK 250.Y PP) are cut out under various angles with respect to the column axis as indicated in Figure 3a. The sections are narrow to precisely impose a flow direction through the structure, but long and several sheets of packing thick to reduce boundary effects (Figure 3b). These cut-outs fit tightly into a wind tunnel of rectangular cross-section (Figure 3c). While conducting air at various known flow rates through the tunnel, the pressure drop over the packing is measured. The results are presented for an exemplary air superficial velocity in Figure 4. Also, the same cut-outs used in the experiments are scanned three-dimensionally in an X-ray CT in order to extract the exact surface structure. From the surface data, a mesh of finite volume elements is created. A CFD calculation of single phase air flow through the packing yields the flow field including the pressure drop. The results are shown in solid symbols in Figure 4.

Measurements and numerical results are in agreement. As expected, the specific pressure drop along the vertical column axis ($\gamma = 0°$) is higher than in direction of the channels. The minimal pressure drop is achieved at an angle around 40° which agrees with the corrugation angle of $\gamma = 42°$. At an angle of around 90°, the pressure drop is higher than at 0°. This is reasonable, since the channels form a narrower angle (84°) with each other when gas is flowing vertically ($\gamma = 0°$) and therefore cause lower flow resistance. For all angles, pressure drop is found to grow with velocity to the power of 1.8.

The approach to scan a packing material and conduct a CFD calculation through the exact packing structure offers a great advantage over experiments: The directional pressure drop data to characterize an anisotropic structure is obtained without actually having to manually cut the packing. Any type of material can be investigated by scanning it in one piece and "virtually" cutting sections out of the resulting 3D mesh.

The CFD calculation through the scanned packing should not be confused with the CFD calculation of the macroscopic flow field using the elementary cell model. The CFD calculation through the scanned packing is possible for single-phase

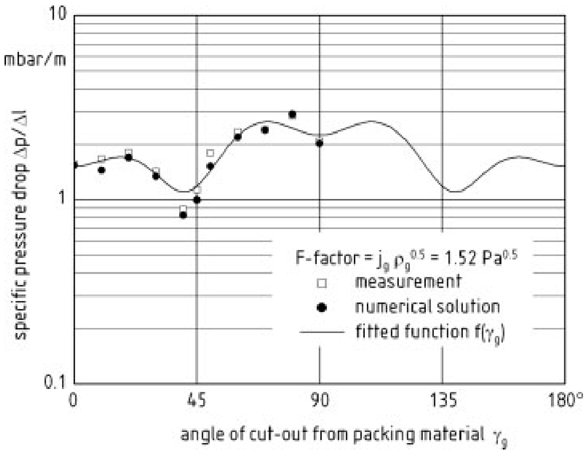

Figure 4. Measurements and numerical results for the anisotropic pressure drop of corrugated structured packing.

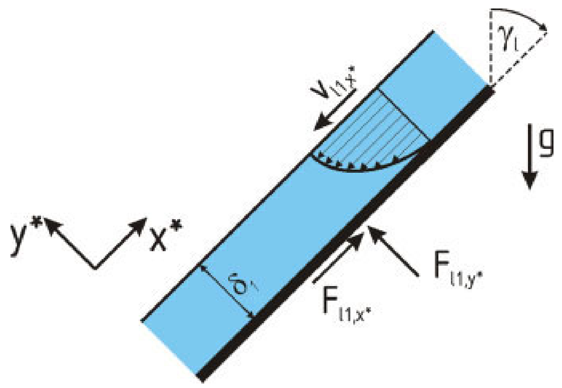

Figure 5. Schematic of laminar film flow on an inclined plate.

[Color figure can be viewed in the online issue, which is available at www.interscience.wiley.com.]

flow and volumes of a few cubic centimeters only. It provides valuable input data for the elementary cell model, though.

From the measurements or numerical CFD results on the packing cut-outs, the anisotropic gas flow resistance tensor $\underline{\underline{\pi}}$ (see Eq. 10) is interpolated as a function of direction and magnitude of gas velocity. The dependency on direction like shown in Figure 4 is interpolated by

$$f(\gamma_g) = \sum_{i=0}^{4} a_i \left[\cos\left(2i(\gamma_g + 48^\circ)\right) + \cos\left(2i(\gamma_g - 48^\circ)\right)\right] \frac{mbar}{m} \tag{23}$$

$$\text{with parameters for } F = 1.52\,\text{Pa}^{0.5} \text{ being} \quad \begin{aligned} a_0 &= 1.83 \\ a_1 &= 2.50 \\ a_2 &= -0.178 \\ a_3 &= 0.263 \\ a_4 &= -0.161 \end{aligned}$$

Numerical results of the macroscopic flow field using the anisotropic flow resistance tensor show that spreading of gas flow from a point source is very well reproduced.

Anisotropic liquid flow resistance

For operating conditions below the loading point, gas-liquid momentum transfer is negligible, and for moderate liquid flow rates laminar film flow can be assumed. The flow resistance tensors $\underline{\underline{\xi_i}}$ for the two modeled liquid phases $i = 1, 2$ [see definitions (17) and (18)] are derived from the laminar film flow model on an inclined plate. Figure 5 shows a schematic of the model exemplary for liquid phase l1.

Assuming a steady-state laminar film, the balance of forces on the film allows to correlate average film velocity $\bar{v}_{li,x^*}$, film thickness δ_i, inclination angle γ and gravity g, yielding

$$\bar{v}_{li,x^*} = -\frac{\rho_l \cos(\gamma) g}{3\,\eta_l} \delta_i^2 \tag{24}$$

In Eq. 24, ρ_l is the liquid density, γ is the inclination angle of the plate measured to the vertical, g is gravity and η_l the liquid viscosity. As indicated in Figure 5, the coordinate and index x^* refers to the direction or component parallel, and y^* normal to the plate. The forces acting from the plate onto the fluid film are F_{li,x^*} parallel and F_{li,y^*} normal to the plate. The shear force F_{li,x^*} acting on the liquid phase i within a control volume V of the column can be written as a function of liquid film thickness,

$$\frac{F_{li,x^*}}{V} = \alpha_{li}\,\rho_l g \cos(\gamma) = \frac{a_p}{2} \delta_i\,\rho_l g \cos(\gamma), \tag{25}$$

where $a_p/2$ is the volume specific surface area of the packing material which is available to liquid phase i. For the elementary cell model, the shear force in Eq. 25 is expressed as a function of the average film velocity (see Eq. 24), giving

$$\frac{F_{li,x^*}}{V} = -\frac{a_p}{2} \frac{\bar{v}_{li,x^*}}{\left|\bar{v}_{li,x^*}\right|} \sqrt{3\,\eta_l \rho_l g \cos(\gamma) \left|\bar{v}_{li,x^*}\right|}. \tag{26}$$

The volume specific normal force is written as a function of the weight of the liquid film and the inertia normal to the plate,

$$\frac{F_{li,y^*}}{V} = \alpha_{li}\,\rho_l g \sin(\gamma) - \alpha_{li} \frac{v_{li,y^*}}{\Delta t} \rho_l. \tag{27}$$

In Eq. 27, Δt is the residence time of the fluid in the control volume. The second expression on the right hand side expresses that all inertia normal to the plate is absorbed. From Eqs. 26 and 27, the flow resistance tensors $\underline{\underline{\xi_i}}$ defined in Eqs. 17 and 18 are formulated.

Interphase momentum transport

For operating conditions below the loading point, the momentum transport at the phase boundary between liquid and gas is negligible. In the loading regime, it cannot be neglected and therefore has to be included in any model which is intended for the full range of operating conditions.

The model employed here is based on the analytical calculation of shear stresses acting on a laminar liquid film in a vertical pipe as described by Brauer.[11] It extends the model of laminar film flow on an inclined plate presented in the previous paragraph. A sketch of a liquid film influenced by the counter-current gas flow is shown in Figure 6. The dimensionless shear stress at the phase boundary τ_δ^* is given by

$$\tau_\delta^* = \frac{\tau_\delta}{g\,\rho_l \delta}, \tag{28}$$

where g is gravity, ρ_l stands for the liquid density and δ for the liquid film thickness. Depending on the dimensionless shear stress, the resulting velocity profiles of gas and liquid are shown schematically in Figure 6b. In order to calculate nonstationary flow fields including potentially arising upward liquid flow, a limitation to counter-current flow shall not be made here.

Assuming that pressure- and accelerating forces are negligible, a force balance leads to the relationship

$$\delta = \delta_0 \frac{1}{\left(1 - \frac{3}{2}\,\tau_\delta^*\right)^{1/3}} \tag{29}$$

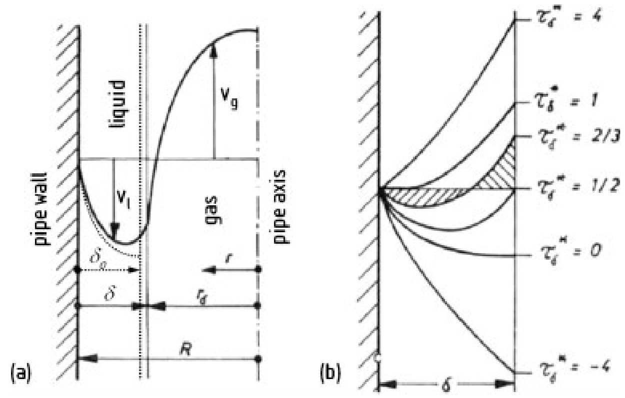

Figure 6. (a) Schematic of gas liquid film flow in a vertical pipe, (b) velocity profile of the liquid film as a function of the dimensionless shear stress at the phase boundary as described by Brauer.[11]

between the liquid film thickness influenced by the gas flow δ and the liquid film thickness with negligible gas flow δ_0. In Eq. 29 it is assumed that the liquid film thickness is small compared to the pipe radius. Taitel et al.[27] prove that this restriction might as well be dropped, since the exact film thickness deviates only marginally from the one calculated with Eq. 29.

Additionally, it is assumed that a minimal liquid film thickness $\delta_{\min}$ exists, under which the film tears open into rivulets. The packing surface wetted by liquid phase i shall be approximated by

$$\frac{a_\mathrm{p}}{2}\chi_i \quad \text{with} \quad \chi_i \equiv \frac{\alpha_{\mathrm{l}i}}{\max\left(\alpha_{\mathrm{l}i},\delta_{\min}\frac{a_\mathrm{p}}{2}\right)}. \tag{30}$$

After rearrangement with the above assumption, one receives

$$\frac{F_{\mathrm{l}i,x^*}}{V} = -\left(\frac{3}{4}\frac{\eta_\mathrm{l}\left(a_\mathrm{p}\chi\,\rho_\mathrm{l} g\cos(\gamma_\mathrm{l})\right)^2 j_{\mathrm{l}i,x^*}}{1-\frac{3}{2}\tau^*_\delta}\right)^{1/3}. \tag{31}$$

Equation 31 replaces Eq. 26 which was valid only for operating conditions below the loading point. The denominator of the right hand side of Eq. 31 describes how the liquid film thickness grows due to gas flow. The dimensionless shear stress at the phase boundary is calculated from the pressure gradient. Equation 31 includes the forces on both sides of the liquid film, namely shear stress at the packing surface and shear stress at the phase boundary with the gas phase.

Implementation

The model is implemented in the commercial software package CFX 10.0 to calculate the counter-current two-phase flow of water and air. Three continuous Eulerian phases are employed to model one gas phase and the two liquid phases. The phases are water and air at 25°C. The modeled packing is SULZER MELLAPAK 250.Y made from polypropylene. It features a corrugation angle of 42° and a specific surface area of 250 m^2/m^3.

The three-dimensional numerical mesh shown in Figure 7 comprises 67,000 volume elements. It represents a column of 960 mm height with 288 mm inner diameter. The column contains four elements of packing, which are rotated against each other by 90°. An effective corrugation angle of 19° is used for the liquid phases. The effective corrugation angle results from the three-dimensional inclination of the packing surface and can be analytically derived.[13] The channels created by the corrugations are oriented at an angle of 42° to the vertical. The channels themselves have a triangular cross-section: the walls of the channels are inclined by 43° against the packing sheet plane. The inclined surface that the liquid sees is a geometric summation of both the channel's orientation and the channel wall's inclination. Therefore, the effective inclination that the liquid follows is much steeper than just the corrugation angle. Projecting the liquid's path along the steepest inclination onto the vertical packing sheet plane yields an angle of 19° between the projected path and the vertical column axis. The projected path is the direction in which you see the liquid flowing in a projection image like the radiography in Figure 9. It should be noted that for the gas phase, these considerations of flow on the inclined plate do not apply. As confirmed by the experimental results, the gas phase is guided along the corrugation angle of ±42°.

Gas and liquid are fed to the column via mass source terms within the numerical grid below, respectively above the packed section, like e.g., for an absorption or desorption process. The phases leave the column at the top, respectively bottom face of the column, where outlet boundary conditions are applied. Calculations are performed on a Dell PWS 650 PC with dual Xeon 2.8 GHz processors and on an IBM pSeries 690 supercomputer of the HLRN (High Performance Computing Network of Northern Germany) at the Regional Computing Cluster of Lower Saxony in Hannover.

Results and Discussion

Figure 8 shows numerical results of the three-dimensional column model. Liquid is fed from a point source just above

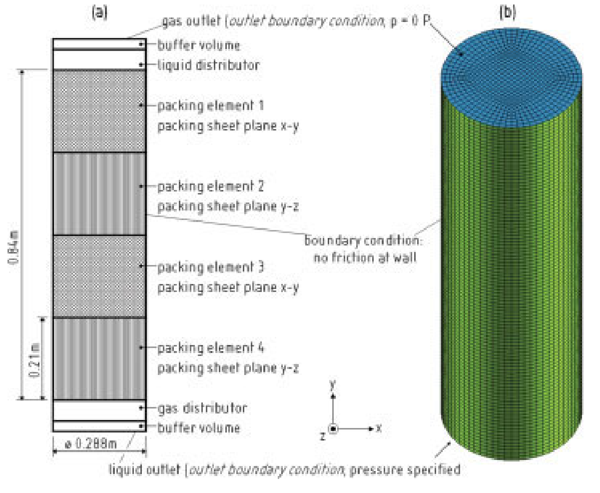

Figure 7. Mesh used for numerical calculations.

[Color figure can be viewed in the online issue, which is available at www.interscience.wiley.com.]

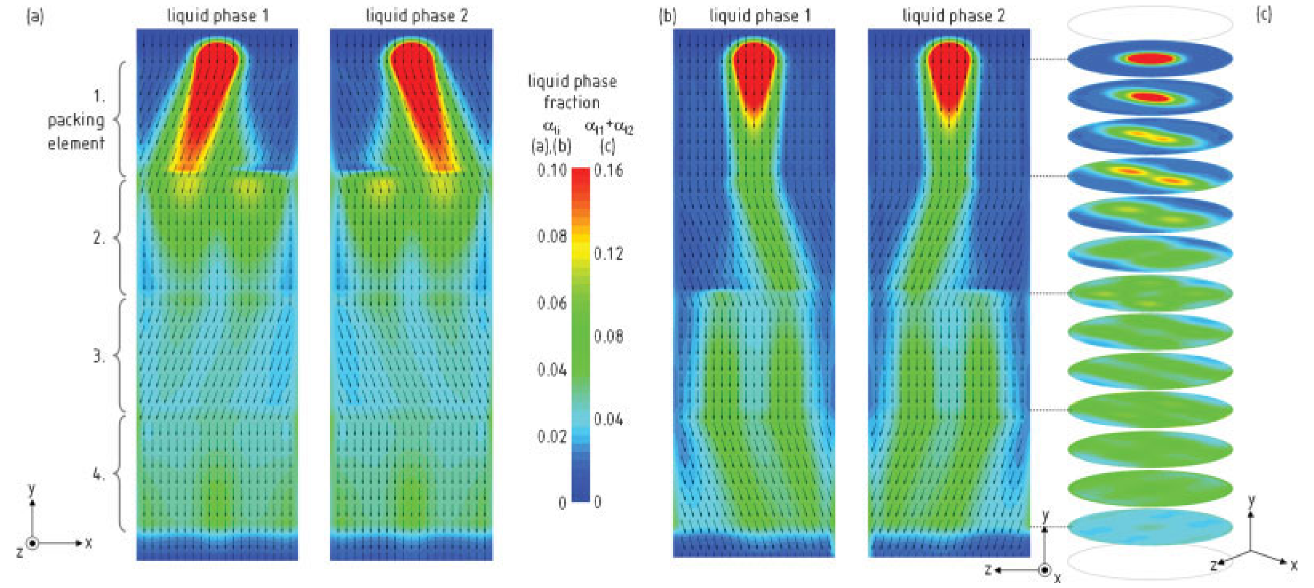

Figure 8. **Numerical result for liquid fed from a point source at 40 $m^3/(m^2\ h)$ and $F = 0.8\ Pa^{0.5}$ (a) vertical *x-y* plane, (b) vertical *y-z* plane, (c) horizontal *x-z* planes.**

the packed section. The liquid flow rate corresponds to a liquid superficial velocity of $j_l = 40\ m^3/(m^2\ h)$, the F-factor of the gas phase is $F = 0.8\ Pa^{0.5}$, which is well below the loading regime. The packed section comprises four packing elements each rotated by 90° around the column axis. In Figures 8a, b vertical planes through the column are visualized. The liquid phases' volume fractions and velocity vectors are shown separately for both modeled liquid phases. In Figure 8a on the left it can be seen how liquid phase 1 is guided from the point source above the top packing element along the preferential flow direction to the left towards the wall. The angle of the velocity vectors is 19° to the vertical, which agrees with the theoretically derived flow direction of the liquid film on an inclined plate mentioned before. Liquid phase 2 flows symmetrically to liquid phase 1 with respect to the vertical. When reaching the joint between packing elements one and two, the liquid is redistributed evenly between both preferential flow directions in the downstream packing element. Because of the 90° rotation of the packing elements, the preferential flow directions in the second packing element are normal to the x-y planes shown in Figure 8a. The spreading in the y-z plane can be seen in Figure 8b. Towards the bottom of the four packing elements, the liquid is distributed uniformly over the column's cross-section. Figure 8c shows horizontal cutting planes through the column color-coded with the total liquid hold-up of both modeled liquid phases. Because of the strong preferential flow directions, most of the liquid is guided along the 19° angle, resulting in two local maxima in liquid phase fraction, as can be seen in the horizontal planes through the first packing element.

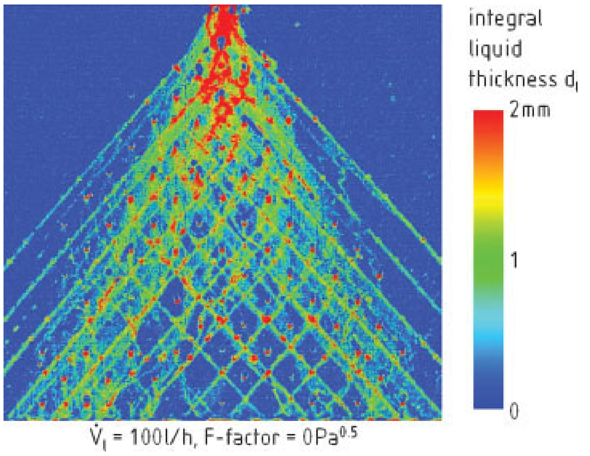

Figure 9. **Spreading of liquid fed from a point-source in between two sheets of MELLAPAK 250.Y (PP) structured packing.**

The integral liquid thickness is measured by X-ray projection.

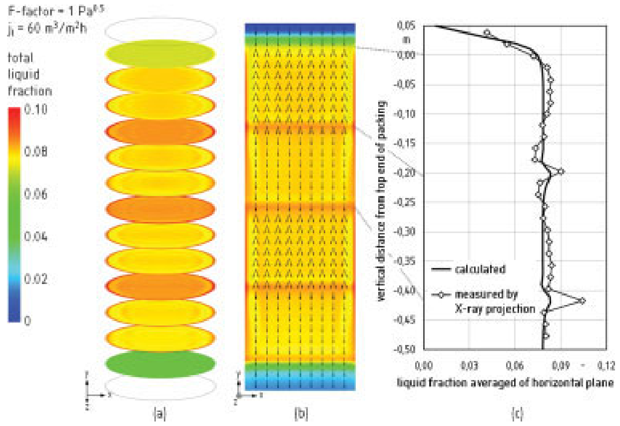

Figure 10. **Numerical result for the 3D-column with uniform liquid irrigation (a) horizontal cutting planes, (b) vertical plane, (c) comparison of calculated and measured liquid phase fraction, averaged over horizontal planes.**

To verify the flow pattern of the liquid through the structured packing, experiments have been conducted with the same type of packing and water as the model fluid. Figure 9 shows an X-ray projection measurement of two sheets of structured packing material. Liquid is fed from two point-sources on the inward-facing surfaces of the two sheets of packing. A liquid film forms on both inner sides of the packing material. The holes in the packing have been sealed in order to keep all liquid in between both sheets. There is no gas flow. The integral liquid film thickness is measured by X-ray projection: A fan beam of X-rays is emitted from the X-ray source. The X-rays are attenuated along their path through the packing material and the liquid. On the opposite side of the test rig, the attenuated X-rays are detected by a line detector. Line-by-line the test-rig is scanned in 0.5-mm intervals giving a full projection image of it. Knowing the X-ray attenuation coefficient of the liquid, the integral liquid film thickness is calculated from the image of the irrigated packing and a reference image of the dry packing using Lambert-Beer's Law. A detailed description of the experimental rig and procedure is found in Mahr and Mewes.[28]

Figure 9 visualizes the result of a projection measurement, where the color indicates the integral liquid thickness. It confirms that at low liquid flow rates most of the liquid is guided mainly along the preferential flow direction of ±19° to the vertical. Only a little liquid is kept in the grooves of the corrugation due to surface tension, and flows along the corrugation angle of ±42° to both sides. In agreement with the numerical result in Figure 8, a local minimum of liquid hold-up is found straight below the injection point.

In Figures 8 and 9 the characteristic test case of a liquid point-source is shown. It also serves as a test case for how the model can deal with extreme maldistribution of the liquid phase. In industrial applications, of course, one always aims at achieving a uniform irrigation. A numerical result for such a case with is presented in Figure 10. Here, the liquid superficial velocity is $j_l = 60$ m^3/(m^2 h) and the F-factor is $F = 1$ Pa$^{0.5}$. The resulting liquid distribution in each cross-section is nearly uniform, see Figure 10a. The velocity vectors in Figure 10b show that the flow direction of the two modeled liquid phases of 19° to the vertical is the same as for the liquid point-source.

In Figure 10c, the calculated and measured liquid fraction averaged over the horizontal plane are plotted against the vertical column coordinate. Around the packing joints, liquid hold-up is considerably higher than within the packing elements. Süess and Spiegel[29] have measured this effect using γ-ray projections for operating conditions above the loading point. Because of its higher spatial resolution, X-ray projection measurements reveal that in a very narrow region around the packing element joints, liquid hold-up is much higher even below the loading point[24] (see Figure 10c). The numerical results shown in Figure 10 reflect this behavior without any model expressions specifically tailored towards it. The elevated hold-up in the numerical results is due to the deceleration of the liquid film, which is caused by the change in orientation of the preferential flow directions and absorption of inertia normal to the packing sheet plane (see Eq. 27).

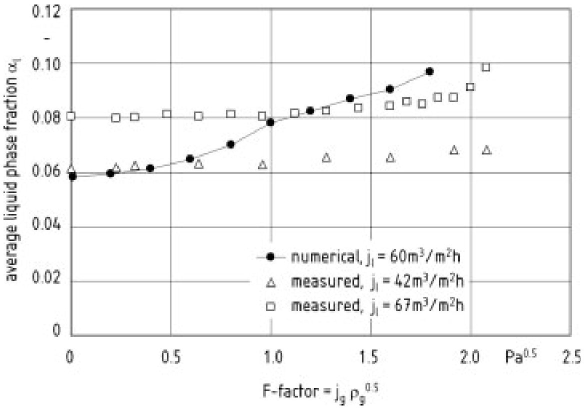

Figure 11. Average liquid hold-up from numerical results and X-ray radiographic measurements, both with uniform liquid irrigation.

For the numerical results presented above, the gas flow rate has always been well below the loading regime. This way, the gas–liquid interaction described by Eq. 31 is included in the model, but it is rather weak and does not lead to instabilities in the flow field, which might be misleading when judging the liquid distribution behavior. To evaluate the impact of the gas–liquid interaction and the robustness of the model at high gas flow rates, calculations with uniform liquid distribution similar to Figure 10 have been conducted for various gas flow rates. Some results are presented in Figure 11 in comparison with experimental results. The measurements were done on a 123-mm I.D. column equipped with MELLAPAK 250.Y (PP) structured packing. Water and air are the model phases and X-ray radiography is used for precise hold-up measurement. For details of the experimental rig and procedure please refer to Mahr and Mewes.[28] The liquid hold-up from both numerical and experimental results is averaged over the packed section and plotted versus the gas flow rate represented by the F-factor. Below the loading point, the gas flow rate has almost no effect on the liquid hold-up. The measurement data for j_l = 67 m^3/(m^2 h) show a constant liquid hold-up up to an F-factor of about 1.3 Pa$^{0.5}$. Above this gas flow rate, the packing is operating in the loading regime where stronger gas-liquid momentum transfer leads to increasing liquid film thickness for increasing gas flow rates. The calculated liquid hold-up is in agreement with the experimental results, which is noteworthy keeping in mind that the model does not contain any empirical parameters fitted to measurement data. The numerical results suggest that liquid hold-up is slightly increasing below the loading point already, though. The model calculates liquid film thickness based on the relation between film thicknesses with and without gas flow as a function of the dimensionless shear stress τ_δ^* at the gas-liquid phase boundary (see Eq. 29 and Figure 6). For this function, the counter-current flow region starts at $\tau_\delta^* = 0$ (i.e., quasi-zero gas flow), and here already the gradient of Eq. 29 has a value greater than zero. Therefore, the model calculates an increasing film thickness and thus growing liquid hold-up even for small gas flow rates. In reality, though, the assumption for the model, that the liquid film is spread evenly over the entire packing's surface with constant thickness, is not quite correct. A considerable fraction of the liquid flows as rivulets in the grooves of the packing corrugations, or it forms fluid bridges at the contact points between two sheets of packing

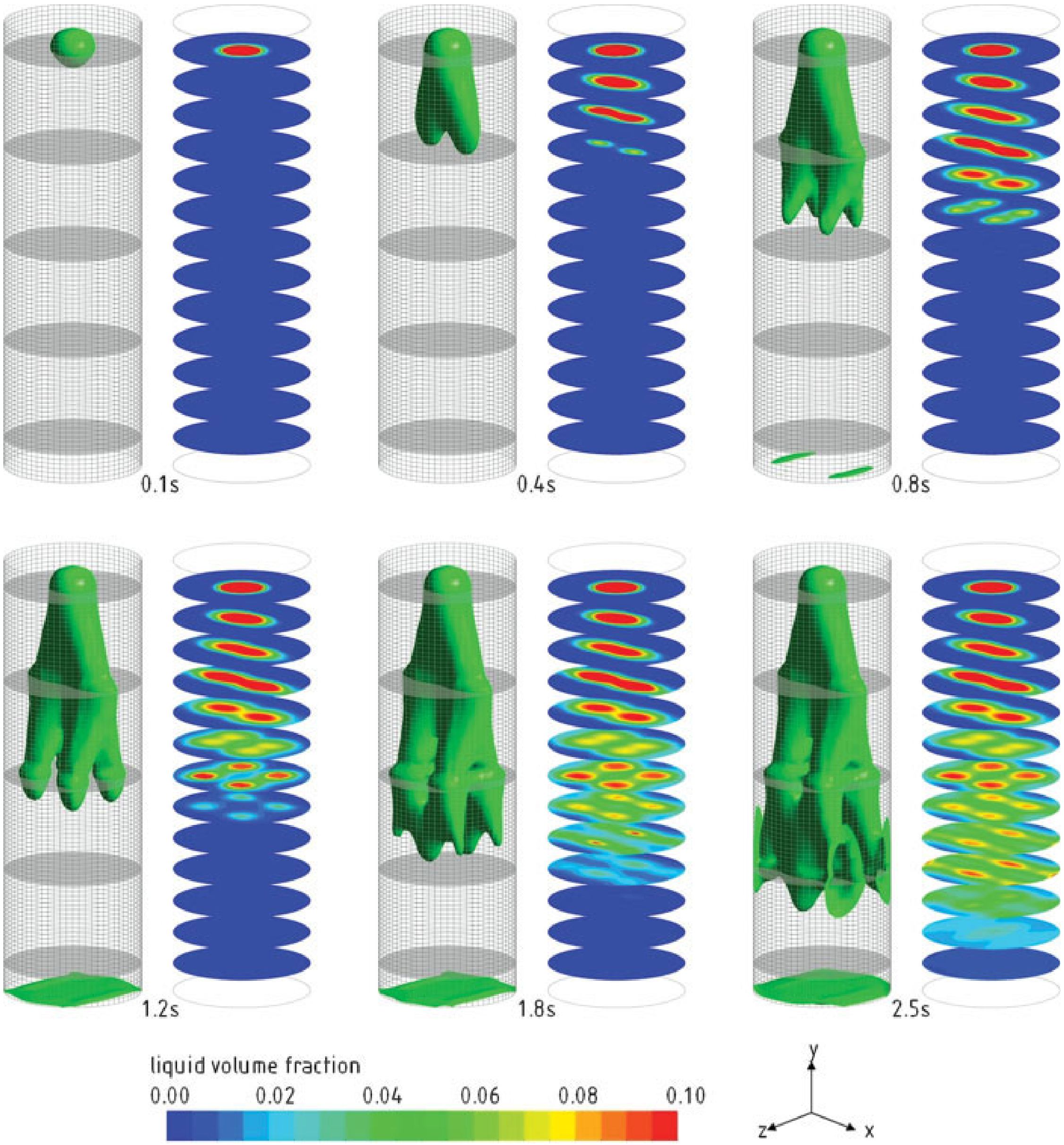

Figure 12. Numerical result for nonstationary boundary conditions.

At $t = 0$, liquid is fed from a point source [$j_l = 40$ m^3/(m^2 h)] at the column head into the gas-filled column ($F = 0.8$ Pa$^{0.5}$). For each time step, the total liquid hold-up is visualized in horizontal planes on the right, and an iso-surface of the total liquid hold-up $\alpha_l = 0.055$ is presented on the left.

material (cf. Figure 9). In these cases, the effect of gas flow on liquid hold-up is much smaller than for a smooth liquid film. Therefore, theory over-predicts the effect of gas flow on liquid hold-up for low gas flow rates.

Above a gas flow rate of $F = 1.6$ Pa$^{0.5}$, which is in the loading regime towards the flood point, the slope of the calculated hold-up curve increases in accordance with measurement data. Calculations for $F = 2.0$ Pa$^{0.5}$ show that the flow field is not stable any more. Especially at the packing elements' joints, liquid velocity vectors are not facing uniformly downwards like for lower gas flow rates. This indicates that the model correctly predicts the onset of flooding. It should be pointed out again that the model does not contain any empirical correlation for loading or flood point prediction. For operating conditions close to the flood point, time steps have to be chosen very small, but with some more work on robust convergence, the model seems to be well suited to calculate highly unstable flow conditions over a longer period of time as well.

So far, all presented numerical results are for stationary flow conditions. The model's ability to calculate non-stationary flow fields is demonstrated in Figure 12. Figure 12 shows a time series of results for a flow field that is dynamic due to time-dependent boundary conditions for the liquid feed. At $t = 0$, liquid is fed from a point source at the column head into the empty, i.e., gas-filled column. The liquid superficial velocity averaged over the column's cross section is $j_l = 40$ m^3/(m^2 h), the F-factor of the gas phase is $F = 0.8\ \mathrm{Pa}^{0.5}$. For each time step, on the left side an iso-surface of the liquid volume fraction $\alpha_l = 0.055$ is shown. On the right side, horizontal planes through the packing elements are visualized. The color scale refers to the liquid volume fraction. In the first packing element, the liquid spreads along the two preferential flow directions producing two regions of local maximum liquid hold-up like in Figure 8. Because of the rotated orientation of the second packing element, each region again splits up into two regions of local maximum liquid hold-up. This results in four regions of local maximum liquid hold-up at the joint between the second and third packing element. Also, the liquid hold-up around the packing joint is slightly higher, as can be seen for example at $t = 1.8$ s. As can be seen from the time-series, the liquid velocity is the highest along the preferential flow directions. In the third packing element, the iso-surface of the liquid volume fraction $\alpha_l = 0.055$ extends to the column wall. Although the preferential flow directions still influence the liquid flow field in the fourth packing element, the liquid distribution is fairly uniform here.

The calculated flow field is dynamic due to the time-dependent boundary condition for the liquid feed at the column head. The flow field is stable, though, which can be seen from the constant liquid distribution e.g., in the first packing element for $t \geq 0.8$ s. An unstable, dynamic flow field would be expected only for operating conditions close to and above the loading point. The presented results confirm that the model is well suited for to calculate dynamic flow conditions even with extreme maldistribution of the phases. With increasing gas flow, the model predicts increasing liquid hold-up,[24] and preliminary results confirm that around the loading point, the model correctly predicts liquid flow direction changing from downward to upward in parts of the column. This indicates that the presented model will be able to capture unstable operating conditions as well.

Conclusions

The elementary cell model is extended to model two-phase flow through structured packings. The anisotropic flow resistance is modeled by a directional pressure drop for the gas phase. Two liquid phases are used to model radial liquid spreading based on a laminar film flow assumption. The interphase momentum transfer is accounted for by an analytical expression. The model is implemented for a three-dimensional column of 0.84 m packed height. It contains four elements of MELLAPAK 250.Y structured packing, each rotated by 90° against each other. For this mesh, steady-state and dynamic flow fields for counter-current flow of water and air are calculated. For liquid fed from a point source, its calculated spreading pattern agrees well with X-ray projection measurements of a quasi two-dimensional experimental set-up. Elevated liquid hold-up is observed at the packing elements' joints. The model promises to be easily used to calculate flow fields in columns at an industrial scale. It is suited for extreme maldistribution of the liquid phase and promises to be applicable to unstable flow conditions as well.

Acknowledgments

The authors like to thank the High Performance Computing Network of Northern Germany (HLRN) at the Regional Computing Cluster of Lower Saxony (RRZN) in Hannover for their kind support and making the computational facilities available (project code nii00023). The packing for experimental work has been kindly provided by Sulzer Chemtech (Winterthur, Switzerland).

Notation

a = specific surface ($\mathrm{m}^2\ \mathrm{m}^{-3}$)
A = area, cutting plane (m^2)
D = volume specific momentum transfer ($\mathrm{kg\ m}^{-2}\ \mathrm{s}^{-2}$)
F = force (N)
g = gravity ($\mathrm{m\ s}^{-2}$)
$\vec{j} = (j_x, j_y, j_z)$ = superficial velocity vector ($\mathrm{m\ s}^{-1}$)
K = linear mass exchange coefficient (−)
$\vec{n}$ = vector normal to surface (−)
p = pressure (Pa)
t = time (s)
Δt = residence time (s)
$\vec{v} = (v_x, v_y, v_z)$ = velocity vector ($\mathrm{m\ s}^{-1}$)
$\vec{\bar{v}} = (\bar{v}_x, \bar{v}_y, \bar{v}_z)$ = average velocity vector ($\mathrm{m\ s}^{-1}$)
V = volume, control volume (m^3)
$\dot{V}$ = volumetric flow rate ($\mathrm{m}^3\ \mathrm{s}^{-1}$)
x, y, z = cartesian coordinates (m)
x^*, y^* = coordinates parallel and normal to the packing surface, respectively (m)

Greek letters

α = phase volume fraction (-)
$\overline{\alpha}$ = average phase volume fraction (-)
δ = liquid film thickness (m)
ε = void fraction (-)
γ = inclination angle of plate or corrugation, measured to vertical (rad)
χ = wetted fraction of packing surface (-)
Γ = boundary of control volume (m^2)
η = viscosity ($\mathrm{kg\ m}^{-1}\ \mathrm{s}^{-1}$)
$\underline{\underline{\pi}}$ = flow resistance tensor of the gas phase ($\mathrm{kg\ m}^{-2}\ \mathrm{s}^{-1}$)
ρ = density ($\mathrm{kg\ m}^{-3}$)
$\underline{\underline{\sigma}}$ = stress tensor ($\mathrm{N\ m}^{-2}$)
$\underline{\underline{\tau}}$ = shear stress tensor ($\mathrm{N\ m}^{-2}$)
$\underline{\underline{\zeta}}$ = flow resistance tensor of the liquid phase ($\mathrm{kg\ m}^{-2}\ \mathrm{s}^{-1}$)

Subscripts

EC = elementary cell
f = free or void fraction
g = gas phase
gl/gl1/gl2 = between gas and liquid/between gas and liquid phase 1/between gas and liquid phase 2
i = index of phase, i = g, l1, l2
k = index of coordinate direction, $k = x, y, z$
l/l1/l2 = liquid phase/liquid phase 1/liquid phase 2
l1 p/l2 p = between liquid phase 1 and packing/between liquid phase 2 and packing
p = packing
t = of the effectively transferring or originating liquid phase

Literature Cited

1. Brunazzi E, Paglianti A. Mechanistic pressure drop model for columns containing structured packings. *AIChE J*. 1997;43:317–327.
2. Dudukovic MP, Larachi F, Mills PL. Multiphase reactors—revisited. *Chem Eng Sci*. 1999;54:1975–1995.
3. Spiegel L, Meier W. Distillation columns with structured packings in the next decade. *Trans IChemE Part A: Chem Eng Res Des*. 2003; 81:39–47.
4. Billet R, Schultes M. Prediction of mass columns with dumped and arranged packings—updated summary of the calculation method of

Billet and Schultes. *Trans IChemE Part A: Chem Eng Res Des*. 1999; 77:498–504.

5. Iliuta I, Petre CF, Larachi F. Hydrodynamic continuum model for two-phase flow structured-packing-containing columns. *Chem Eng Sci*. 2004;59:879–888.
6. Olujic Z, Kamerbeek AB, de Graauw J. A corrugation geometry based model for efficiency of structured distillation packing. *Chem Eng Proc*. 1999;38:683–695.
7. Stichlmair J, Bravo JL, Fair JR. General Model for prediction of pressure drop and capacity of countercurrent gas/liquid packed columns. *Gas Sep Purif*. 1989;3:19–28.
8. Billet R. *Packed Towers in Processing and Environmental Technology*. Weinheim: VCH Verlag, 1995.
9. Kister HZ. *Distillation Design*. New York: McGraw-Hill, 1992.
10. Rocha JA, Bravo JL, Fair JR. Distillation columns containing structured packings: a comprehensive model for their performance, Part 1: Hydraulic models. *Ind Eng Chem Res*. 1993;32:641–651.
11. Brauer H. *Grundlagen der Ein- und Mehrphasenströmungen*. Aarau: Sauerländer Verlag, 1971.
12. Stoter F, Olujic Z, de Graauw J. Modelling and measurement of gas flow distribution in corrugated sheet structured packings. *Chem Eng J*. 1993;53:55–66.
13. Stoter F. Modelling of Maldistribution in Structured Packings: From Detail to Column Design. Ph.D. Thesis, TU Delft, 1993.
14. Jiang Y, Khadilkar MR, Al-Dahhan MH, Dudukovic MP. Two-phase flow distribution in 2D trickle bed reactors. *Chem Eng Sci*. 1999; 54:2409–2419.
15. Jiang Y, Khadilkar MR, Al-Dahhan MH, Dudukovic MP. CFD of multiphase flow in packed-bed reactors. I. *k*-fluid modelling issues. *AIChE J*. 2002;48:701–715.
16. Iliuta I, Ortiz-Arroyo A, Larachi F, Grandjean BPA, Wild G. Hydrodynamics and mass transfer in trickle-bed reactors: an overview. *Chem Eng Sci*. 1999;54:5329–5337.
17. Mewes D, Loser T, Millies M. Modelling of two-phase flow in packings and monoliths. *Chem Eng Sci*. 1999;54:4729–4747.
18. Arbogast T, Douglas J, Hornung U. Derivation of the double porousity model of single phase flow via homogenization theory. *SIAM J Math Anal*. 1990;21:823–836.
19. Petre CF, Larachi F, Iliuta I, Grandjean BPA. Pressure drop through structured packings: breakdown into the contributing mechanisms by CFD modeling. *Chem Eng Sci*. 2003;58:163–177.
20. Nijemeisland M, Dixon AG. CFD study of fluid flow and wall heat transfer in a fixed bed of spheres. *AIChE J*. 2004;50:906–921.
21. Zhang LZ. Turbulent three-dimensional air flow and heat transfer in a cross-corrugated triangular duct. *Trans ASME: J Heat Transfer*. 2005;127:1151–1158.
22. Hoffmann A, Ausner I, Repke JU, Wozny G. Detailed investigation of multiphase (gas-liquid and gas-liquid-liquid) flow behaviour on inclined plates. *Trans IChemE Part A: Chem Eng Res Des*. 2006; 84:147–154.
23. Loser T. Berechnung der zweiphasigen Strömung in Schichtungen. Ph.D. Thesis, Institut für Verfahrenstechnik, Universität Hannover, 2002.
24. Mahr B. Numerisches Berechnen und tomographisches Messen zweiphasiger Strömungsfelder in geordneten Schichtungen. Ph.D. Thesis, Institut für Mehrphasenprozesse, Leibniz Universität Hannover, 2007.
25. Mahr B, Mewes D. Modelling and measurement of macroscopic flow fields in structured packings. Prodeedings of the 8th Distillation and Absorption Conference. London, UK, 2006.
26. Mahr B, Mewes D. CFD modelling and calculation of dynamic two-phase flow in columns equipped with structured packing. *Trans IChemE Part A: Chem Eng Res Des*. 2007;85:1112–1122.
27. Taitel Y, Barnea D, Dukler AE. A film model for the prediction of flooding and flow reversal for gas-liquid flow in vertical tubes. *Int J Multiphase Flow*. 1982;8:1–10.
28. Mahr B, Mewes D. X-ray tomographic visualization of liquid spreading in structured packings using a contrast-agent tracer. Prodeedings of the International Heat Transfer Conference IHTC-13. Sydney, Australia, 2006.
29. Süess P, Spiegel L. Hold-up of Mellapak structured packings. *Chem Eng Proc*. 1992;31:119–124.

Manuscript received July 3, 2007, and revision received Nov. 7, 2007.